applied sciences

MDPI

Article

Resonant Fatigue Tests on Drill Pipe Connections with Different Geometries and Sizes

Ciro Santus [1], Lorenzo Romanelli [1,*], Alessandro Burchianti [2] and Tomoya Inoue [3]

[1] Department of Civil and Industrial Engineering—DICI, University of Pisa, Largo Lucio Lazzarino 1, 56122 Pisa, Italy; ciro.santus@unipi.it
[2] ACTA Srl, Via della Villana 154, 57016 Livorno, Italy
[3] Engineering Department, JAMSTEC—Japan Agency for Marine-Earth Science and Technology, Yokosuka 238-8550, Japan
* Correspondence: lorenzo.romanelli@phd.unipi.it

Abstract: In this study, a resonant bending fatigue test rig, designed and implemented by the University of Pisa, is presented, providing a detailed description of the set-up of the machine, the strain gauges calibrations, and the control system used with the main electronic devices. Several geometries of drill pipe connections and pipe samples made of different materials were tested, and all the obtained experimental fatigue results are presented in the paper and compared to previous experimental data. Fractographic images are provided to clearly show that, in two kinds of drill pipe connections, the crack initiation was found at the connection zone, whereas for another connection geometry, it was found at the pipe body. In order to interpret these latter results, a discussion about the section modulus of bending of the various sections of the drill pipes was provided, along with an FE model of a specific zone of one of these connections.

Keywords: drill pipe connection; resonant bending fatigue test; strain gauge; upset region; pipe body

check for updates

Citation: Santus, C.; Romanelli, L.; Burchianti, A.; Inoue, T. Resonant Fatigue Tests on Drill Pipe Connections with Different Geometries and Sizes. *Appl. Sci.* **2023**, *13*, 8006. https://doi.org/10.3390/app13148006

Academic Editors: Ricardo Branco, Joel De Jesus and Diogo Neto

Received: 9 June 2023
Revised: 30 June 2023
Accepted: 6 July 2023
Published: 8 July 2023

1. Introduction

Drill pipes are the main components of a drill string, which is the long tubular structure that connects the drilling bit to the rig. The dimensions of the rotary drilling elements are defined by the American Petroleum Institute (API) standard [1]. Drill strings can be used for oil exploration, but they can also be employed for scientific drillings, as utilized by JAMSTEC on the drilling-equipped science vessel Chikyu. As described in refs. [2,3], these long tubular elements can serve to investigate the most active earthquake zones near the Japanese coasts.

The two mating parts of a drill pipe, named, respectively, the “pin” and the “box” tool joints, are connected through a conical threaded connection with single or double shoulder seal faces. The connection zone is characterized by a larger external diameter and a smaller internal diameter with respect to the pipe body. An intermediate region (upset) is required to provide the attachment, generally realized through a friction welding process, between the pipe body and each tool joint to smooth the stress distribution at the transition from the threaded zone to the pipe body. A drill pipe is so generally composed of three parts: the connection, the upset, and the pipe body. As resumed in ref. [4], in drill pipes there are some stress concentration points, which can be classified as:

- Surface irregularities,
- Section variation at the upset,
- Corrosion pitting,
- Stress concentrations at the threaded region.

The surface irregularities can be caused by inappropriate handling with the gripping systems or by slip-cuts. In refs. [5,6] the stress concentration effects caused by the die-marks on the static and fatigue failures were investigated. Alternatively, the upset zone can be a potential point of cracking in a drill pipe. In ref. [7], the erosion caused by the drilling fluid on the internal upset was examined using the CFD software FLUENT 13.0 to obtain the shear stress and the pressure at the contact between the fluid and the upset in order to investigate the flow erosion. In ref. [8], a stress analysis of the upset region was conducted through an FE software, and a geometric optimization of this zone was proposed. In ref. [9], an FE simulation of the upset region was developed trying to understand which are the geometric features with the most impact on the stress distribution of the upset region. The authors eventually developed an optimized geometry for the upset region of the 5″ connection according to the API drill pipe standard [1].

Corrosion pitting is generally caused by the removal of the internal coating caused by the drilling fluid, which exerts an erosive impact. This issue was investigated in ref. [10], where it was stated that the irregularities of the internal surface and the employment of a material with a low resistance to corrosion could have a significant impact on failure due to corrosion. The threaded connection zone of the drill pipe received great interest from the researchers. In ref. [11], FE simulations were carried out, showing that the maximum stress concentration factor occurred at the root of the first engaged thread (FET) of the pin and at the last engaged thread (LET) of the box. The simulations aimed to reproduce the preload, the axial load, and the bending load caused by the dog-leg imposed bending, which severely deteriorate the fatigue strength of the drill pipe [12]. In ref. [11], fractographic observations of the failed drill pipes were also included, showing that the crack nucleated at the first thread root of the pin and propagated through the wall of the tool joint. Several other research papers showed that the first and the last engaged threads of the pin and the box, respectively, are potential sites of failure [13–19]. In ref. [20], a method to predict the fatigue life of the threaded connection of drill string was proposed. This latter included a preliminary study to assess the stress tensor at the first and the last engaged threads of the connection, and the Dang Van criterion was then used to calculate the fatigue strength. Although the use of a purely elastic constitutive law, the authors suggested that the eventual elastic-plastic behavior of the most stressed thread roots during the cyclic loading should be investigated. This last proposal can be accomplished following two different methods: the first would employ FE simulations while the second would make use of closed-form expressions as the Neuber rule or the Zarka rule [21]. Other analyses of the threaded connection [22,23] were also carried out on the drill collar, where the connection is clearly the weakest point given that the pipe body has the same inner and outer diameters of the threaded zone. In ref. [23] it was highlighted the strong influence of the make-up load on the mean and on the alternating stress of the FET of the pin because a high make-up torque led to a later contact loss so, given that this thread generally experiences the maximum bending load, a lower alternating stress. Careful monitoring of the make-up operation is recommended for fatigue initiation prediction. After these studies related to the connection, some geometric optimizations were discussed in order to reduce the stress concentration factors of this region, as in [14–16,24,25], and in ref. [26] it was proposed to generate, through an over-make-up torque, a controlled compressive state at the most stressed zone of the connection. The various mentioned stress concentrations can be crucial for the fatigue strength, which is the main cause of failure for drill pipes, as stated in refs. [4,18,27–30]. In addition to this, the vibration of the drill string can result in further fatigue damage, and there are three principal mechanisms of vibration: bit bounce (axial), stick/slip (torsional), and lateral (bending). Various approaches can be used to analytically model the dynamic behavior, in ref. [31] the differential quadrature method was used, in ref. [32] a model that included axial and torsional drill string dynamics and the damping of the structure was performed to investigate the stick-slips vibrations, while in ref. [33] a three-DOF model was used to study the torsional vibrations of drill strings. The vibration analysis can be crucial for long drill strings, given that the natural frequency of axial vibration can be close to that of the heave motion, as shown in ref. [34]. In order to reduce the torsional oscillations of the drill strings, the use of Multiple Scales Lindstedt–

Poincaré method was used to design an optimum damper in ref. [35], whereas in ref. [36] an optimized Linear–quadratic–Gaussian control was accurately designed.

In order to experimentally characterize the fatigue strength of drill pipes, it is possible to perform quasi-static tests, as shown in refs. [37,38], whereas in ref. [39] two kinds of resonant fatigue test benches were presented. The first is suitable to test short regions of heavy sections, such as drill collars, and it employs two couples of counter-rotating eccentric masses, providing an in-plane alternating bending on the tested samples. The second is generally used to test long tubular specimens as drill pipes by means of a single rotating eccentric mass at one end, along with two fixed masses at both ends. The rotation of the eccentric mass provides a rotating bending, which in principle, is quite small according to a quasi-static analysis. However, in both kinds of these test rigs, the eccentric masses rotate at a frequency near (but lower) than that corresponding to the first natural frequency of the structure. These two proposed resonant test rigs were able to reproduce a fully alternating load ($R = -1$), so the mean stress was null. The second idea of the resonant fatigue test was also applied in other research regarding pipes, as in refs. [40–43]. Moreover, the concept of exploiting the resonance to obtain fatigue failure was employed to test various other mechanical components. In ref. [44], a resonant bending fatigue test for large-scale structural components, in particular a railway, was presented, showing a lower duration and a lower energy cost than a quasi-static hydraulic test. An interesting point of this proposed test rig was that the authors made use of springs to also apply a mean stress to the tested samples. Another resonant bending test was applied to marine risers connected by a flange joint in ref. [45] and by welding in ref. [46]. In addition to this, in ref. [47], a biaxial resonant test method was exploited to simultaneously perform fatigue tests on a wind turbine blade in the flap and edge direction, and in ref. [48] a novel rotor blade fatigue test set-up (with elliptical biaxial resonant excitation) was proposed. Nevertheless, not only large-scale components can be tested in this way; in fact, the concept of a resonant test rig can be applied to assess the fatigue strength of small-scale specimens too. For example, in ref. [49], a vibration-based test was proposed on small specimens. The sample was jointed to the shaker armature through a specially designed support, and a successful validation of the equipment was conducted on specimens of 6061-T6 under fully reverse bending. In ref. [50], a computerized electrodynamic resonant fatigue test machine was employed to assess the fatigue strength of automotive components, such as crankshafts and in ref. [51] a resonant plate test bench with I-beam topology was used to reduce the time related to shaft testing. This kind of test can even be applied for structures that are outside of the field of mechanical engineering, such as in ref. [52], where resonant fatigue tests were conducted on samples of concrete. Other examples can be found in ref. [53] to obtain the bending fatigue properties of Polycarbonate and in ref. [54] to characterize the fatigue behavior of a medical rehabilitation exoskeleton device. In this study, the resonant bending fatigue test rig designed by the University of Pisa in collaboration with ACTA Srl is initially presented, including a global overview of all the principal components of the machine, such as the control system, the employed electronic devices, and the strain gauges calibrations. After that, four types of drill pipe geometries tested on this test rig are introduced, and the experimental fatigue strength results of their corresponding samples are shown. Finally, a discussion to interpret the main causes behind the locations of the fatigue crack initiation is provided with some suggestions for further research.

2. Materials and Methods

2.1. Description of the Resonant Test Rig

The test rig designed by the University of Pisa, in collaboration with ACTA Srl, is shown in Figure 1. Two supports were settled at the two nodes of the first natural frequency of the structure, so they were only functional to support the weight of the pipe. Two fixed masses were added to reduce the first natural frequency of the structure. In order to obtain this, an alternative solution was to make the drill pipe longer instead of adding mass, but this was difficult to accomplish. An asynchronous electric motor, driven by an inverter, spun an eccentric mass at a frequency near to that of the first natural frequency of (bending) vibration of the drill pipe. The link between the electric motor and the eccentric mass featured homokinetic joints to freely allow angular and displacement misalignment. Pictures of the two lasers employed to measure the horizontal and vertical displacements at a specific location and about the rotating mass during the motion are shown in Figure 1b,c, respectively.

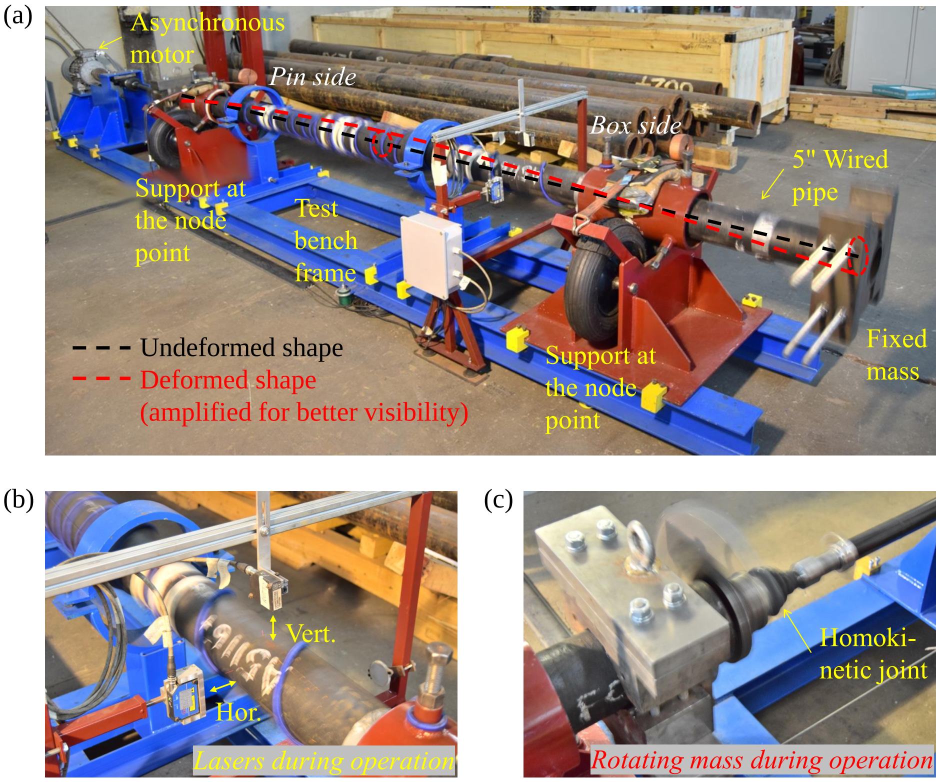

Figure 1. (**a**) Test rig during testing operation, (**b**) laser sensors to measure the horizontal and vertical displacements while vibrating, (**c**) eccentric rotating mass during testing operation.

An FE model, obtained with the Ansys Workbench software 2021 R2 was performed to find the correct lengths of the two sides of the drill pipe and then the positions of the two nodes corresponding to the first natural frequency. The correct lengths of the two sides were set to have the same stress values at the two referenced points in Figure 2. These two points are in correspondence with the strain gauges locations, which will be described below.

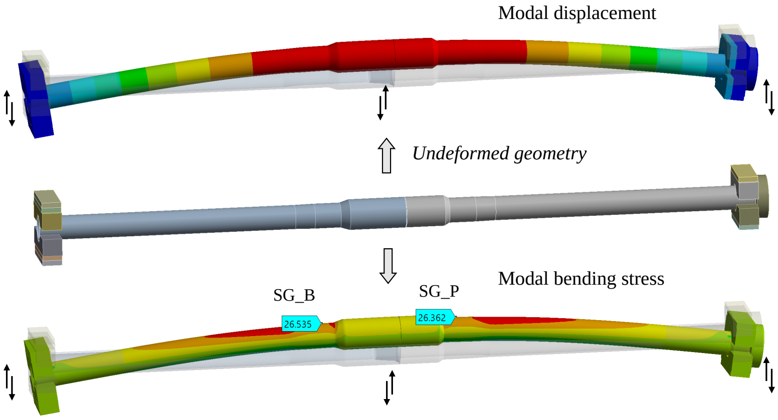

Figure 2. Bending displacement and stress, obtained through FE simulation, corresponding to the first natural frequency vibration modal shape.

2.2. Calibration of the Strain Gauges and Laser Signal Set Up

The main signal to control during the tests was the alternating stress at a point of the pin or at a point of the box close to the connection edge. These two values would nominally be the same, but some differences generally occurred for experimental reasons or geometry inaccuracies. For this reason, the controlled quantity during the tests was the average between the alternating stresses at the pin and box strain gauges' locations. Therefore, the calibration of the strain gauges was crucial in order to record reliable values of the stresses. During this operation, the static load was applied through a hydraulic actuator, and the load cell at the end of the actuator was previously calibrated. The positions of the applied load and of the supports were accurately recorded, and the three strain gauges to be calibrated were set at the pin, at the box, and at the connection, as shown in Figure 3a. Once the static load was applied, the voltage signals of the strain gauges were recorded, and the ratios between the stresses, calculated through the beam theory, and the voltages were evaluated and recorded. These ratios are indeed the conversion factors to be employed during the test, and this was repeated for each sample of the testing campaign. It might be argued that the stress calculated with the beam theory at the connection did not accurately represent the state of stress at this location. However, as explained below, the strain gauge at the connection was not considered as the stress reference of the tests. Nevertheless, it could be employed in case of failure of both the strain gauges at the pin and at the box. The procedure for applying the strain gauges is shown in Figure 3b–d. Given the pulsating load during the tests, the electric wires of the strain gauges were subjected to a push-pull load; thus, in order to enhance their fatigue lives, the fixing process required particular attention. As shown in Figure 3b, they were initially mounted loose, forming an omega shape. Then the strain gauges were glued to the samples using a Teflon tape with a layer of neoprene, which allowed us to uniformly distribute the pressure, during the glue curing, with a thin sheet of metal and two magnets. After that, the two layers of Teflon and neoprene were removed, and a slice of HBM ABM75 was employed, as shown in Figure 3d, to avoid large vibrations of the electric wires during the test. Despite these precautions to avoid the rupture of the electric wires, sometimes the signal had a failure after a certain percentage of the test duration, mainly due to the fatigue of the strain gauge grid. In order to reliably continue the test, the controlled signal was switched on a strain gauge not damaged or on a laser. The measures of the internal and external diameters at the locations of the strain gauges were of fundamental importance in order to perform the correct stress calculations during the strain gauges calibrations. As concerns the internal diameter, a comparator rod was conceived and produced, as shown in Figure 4. The measurement with the internal diameter rod comparator required three steps: first, it was inserted to reach the strain-gauge position; second, through a leverage system, the two adjustable side contacts were pushed until the internal diameter was reached. Then, the diameter span was registered, the comparator was extracted, and the desired measure was finally obtained with a caliper. According to Figure 4c, the alternative way was to cut the samples in correspondence with the strain gauges' locations and to measure the internal diameter, as done for the samples of the second kind of geometry. This operation could only be done at the end of the tests and required a more onerous set-up and a back-calculation of the actual stresses applied during the test. The external diameters were simply measured through the employment of a caliper.

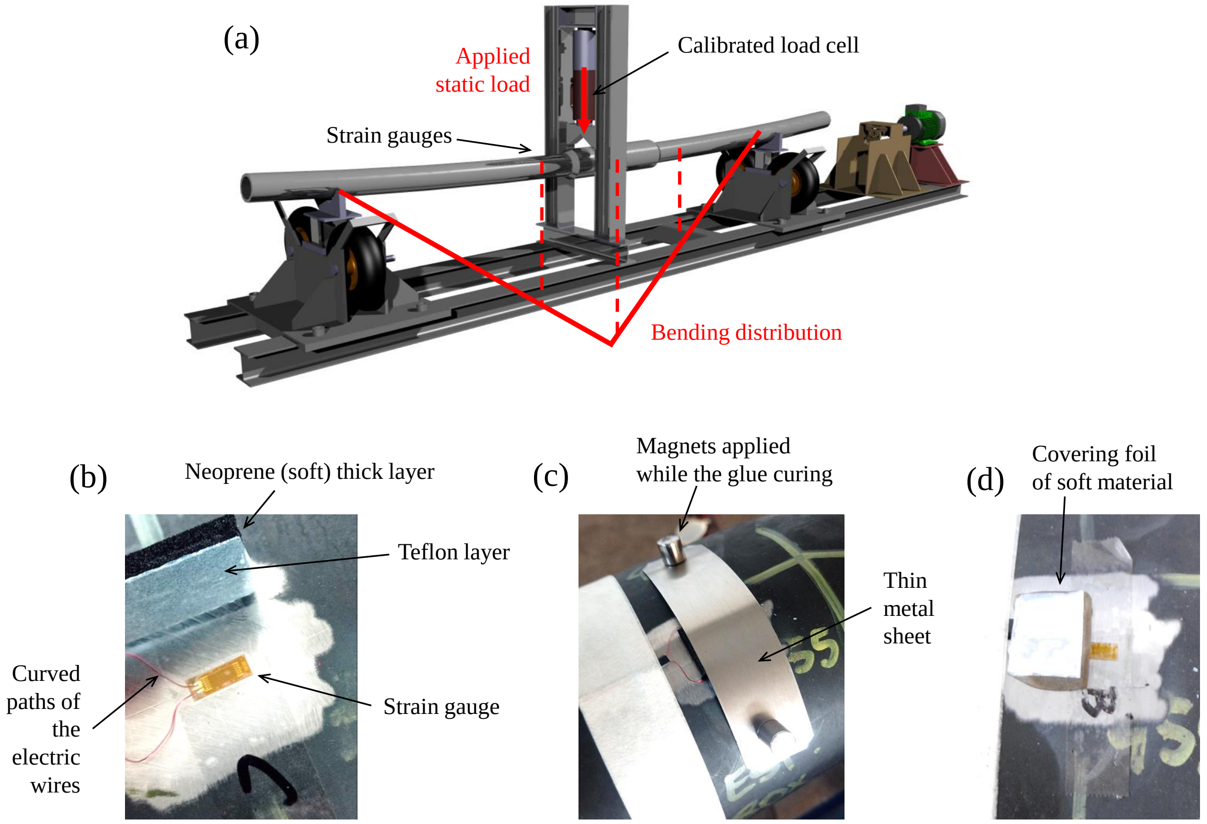

Figure 3. (**a**) Set-up of the test rig during the static calibration of the strain gauges, (**b**) layers of Teflon and neoprene to preliminarily press the strain gauges to the samples, (**c**) employment of a thin sheet of metal to press the strain gauge during the curing of the glue, (**d**) employment of a slice of soft material to stabilize the electric wires.

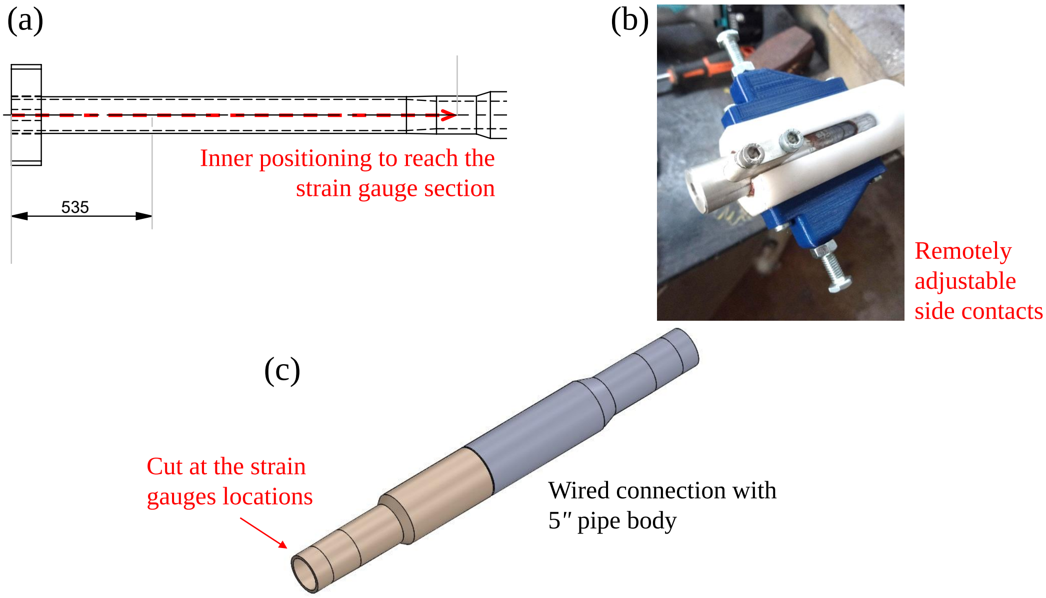

Figure 4. (**a**) Schematic explanation of the insertion of the comparator rod, (**b**) picture of the remotely adjustable side contacts of the comparator, (**c**) cuts at the strain gauges locations to measure the internal diameters.

2.3. Control System to Regulate the Test Rig during the Test

The control system to operate the test rig is shown in Figure 5. The boxes of Figure 5a briefly summarize the logic behind the control system. In the first part of the tests, the objective was to reach the imposed alternating stress at the pin and at the box designed locations, and the voltage signals to perform this task were extracted from the strain gauges. The previously introduced calibration constants for the strain gauges are used during the dynamic run. Given that the experimental stress at the pin and at the box could be slightly different, the average between these two quantities was generally controlled. Once the target value of the alternating stress $\sigma_{\mathrm{a,ref}}$ was reached, the control was kept on the strain gauge acquisition or switched either to the connection strain gauge, or alternatively to the laser displacement signal whenever the strain gauge started to be unreliable. The reference value of the alternating laser displacement $\delta_{\mathrm{a,ref}}$ was registered at the laser position once the alternating stress reached the target value during the initial minutes of the run. The voltage signals obtained from the strain gauges and the lasers were converted to digital and, through the calculated scale factors, the corresponding values of the alternating stress σ_{a} and alternating laser displacement δ_{a} were then obtained. In both situations, the alternating signals were compared with the corresponding desirable values obtaining the related prediction error e, and a Proportional Integrative (PI) control continuously produced a pulse-width modulation (PWM) voltage signal. Given that the inverter was set to work with an analog voltage input, a conversion of the PWM voltage signal to a fixed averaged signal to dialogue with the inverter was required. This last conversion was conducted considering that, generally, during these tests, a small portion of the available scale of the inverter was exploited, so the converted voltage quantity directly fell into this interval in order to enhance the resolution. The inverter output was a power alternating current with a frequency f. However, the working frequency of the motor (f') scaled from that at the inverter (f) by the sliding factor (k), so the excitation frequency of the eccentric mass eventually was f'. In Figure 5b, there is an overview of some of the electronic devices employed during the tests. An ARDUINO card provided the analog-to-digital conversion and vice versa, whereas the ethernet cable allowed to send the information to the control software (on a PC and managed with MATLAB R2021b), where the PI controller was implemented. Finally, on the right of the figure it is shown the card to enhance the resolution of the voltage signal before entering into the inverter.

In Figure 6a, the qualitative trends of the stress obtained at the pin, at the box, and at the connection during a test are reported, whereas in Figure 6b, the qualitative trends of the horizontal and vertical displacements at the laser position are shown, and a phase shift of $\pi/2$ is evident. In Figure 6c the recorded alternating amplitudes during a particular test are presented, and they were obtained as half of the difference between the minimum and the maximum values of the related quantities during the test. Figure 6c, is referred to the type of geometry Connection with 5-1/2×0.415″ pipe body, which will be better introduced below. In the samples belonging to the last mentioned kind of geometry, the desirable alternating stress was not equal to $\sigma_{\mathrm{a,ref}} = 270$ MPa, given that the strain gauges were not located at the pipe body, but they were placed at the upset region.

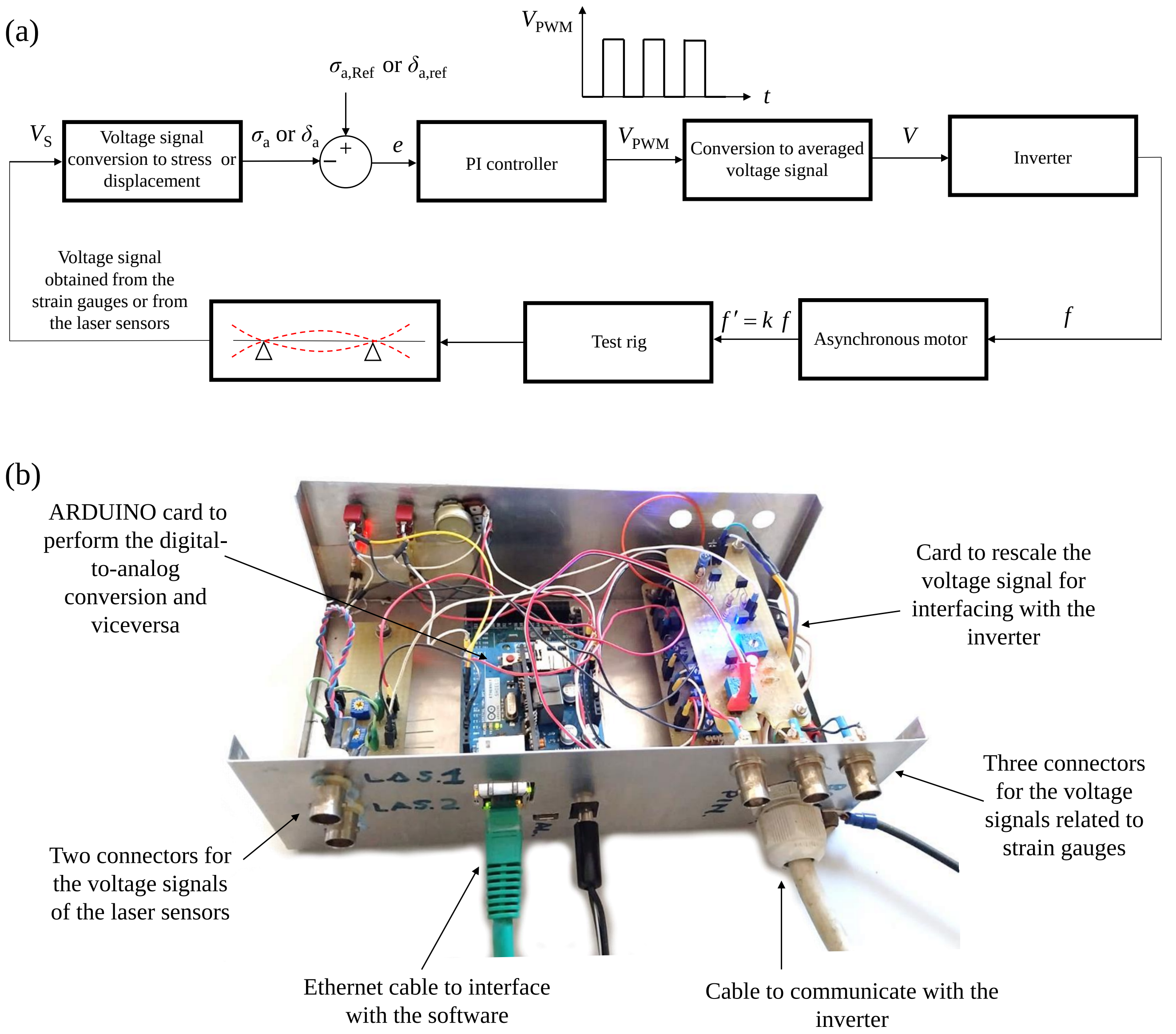

Figure 5. (**a**) Control scheme to explain the driving of the test rig, (**b**) electronic devices employed during the tests.

2.4. Types and Geometries of the Tested Specimens

Five types of geometries were tested by means of the introduced test rig, and their technical drawings are reported in Figures 7 and 8, while the nominal diameters of the various sections of the drill pipes are reported in Figure 9. The nomenclature of the investigated geometries refers to the nominal external diameter and the wall thickness of the pipe body. The first type of geometry was named as Connection with 5-1/2×0.415″ pipe body, and it presented either a regular upset or a longer upset as explained in Figure 7a,b. The second type of geometry, named Wired Connection with 5×0.374″ pipe body, presented an internal hole to accommodate a wire sensor, while the third type of geometry was named Connection with 6-5/8×0.750″ pipe body. Finally, the fourth type of geometry was a pipe specimen 6-5/8×0.750″, for which the test was focused just on the pipe body instead of the connection region. In Figures 7 and 8, the positions of the supports, determined through the FE analysis explained in Section 2.1, and the positions of the strain-gauges are reported. The strain-gauges were not always applied to the pipe body of the drill-pipe as in Figure 7a,b, but at the (pin and box) upset regions instead. This last accommodation of the strain gauges was motivated by the fact that there was not a pipe body zone on one half of the longer upset samples, so the strain gauges were both located at the upset region for uniformity. The third type of geometry presented a heavier section than the other two types with a connection zone. This had an effect on the value of the first natural frequency. Additional fixed masses were thus applied to lower the natural frequency of the structure, as shown in Figure 8. The measured external and internal diameters differ from the nominal values; for example, for a sample belonging to the category Wired Connection with $5 \times 0.374''$ pipe body, the measured external diameter resulted equal to $D_{\text{ext}} = 127.8$ mm, whereas the measured internal diameter was equal to $D_{\text{int}} = 105.8$ mm. In the case of the wired samples, all the measured diameters resulted in a smaller value of the measured internal diameter than the nominal value and a bigger value of the external diameter than the nominal value. The samples of the first kind of geometry were made of AISI 4340 steel, those of the second kind were made of S135 steel grade, with a yield stress of $S_Y = 135$ ksi, and those of the third and fourth kinds of geometry were made of Z140 steel or UD165 steel grades, corresponding to a yield stress of $S_Y = 140$ ksi and $S_Y = 165$ ksi, respectively. The reported values of the yield stress are the minimum guaranteed during the tests.

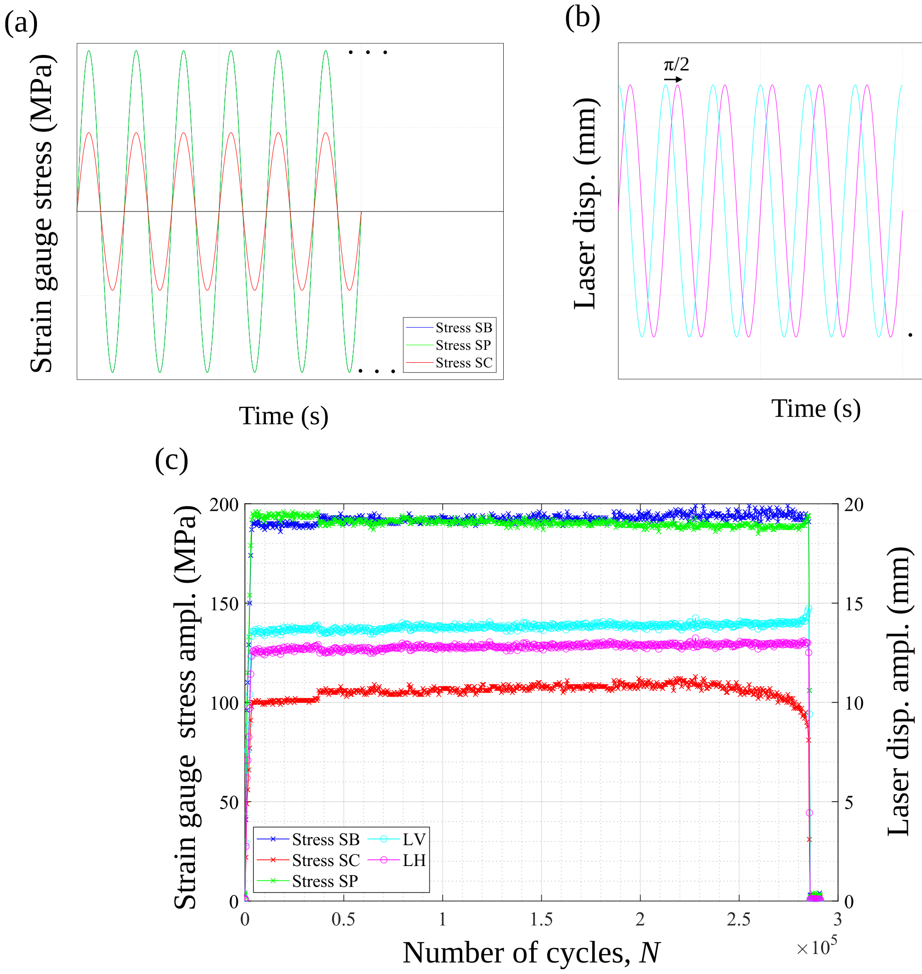

Figure 6. (**a**) Qualitative trend of the stresses during the tests at the pin, at the box and the connection strain gauge locations, (**b**) qualitative trend of the horizontal and vertical displacements obtained by the laser sensors and (**c**) saved stress and displacement amplitudes during one of the tests along the accumulated number of cycles.

(a) Connection with 5-1/2×0.415″ pipe body - AISI 4130 - Regular upset

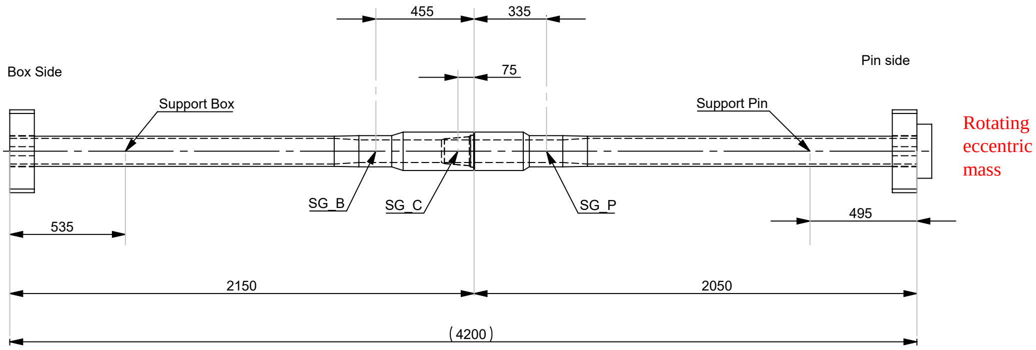

(b) Connection with 5-1/2×0.415″ pipe body - AISI 4130 - Longer upset

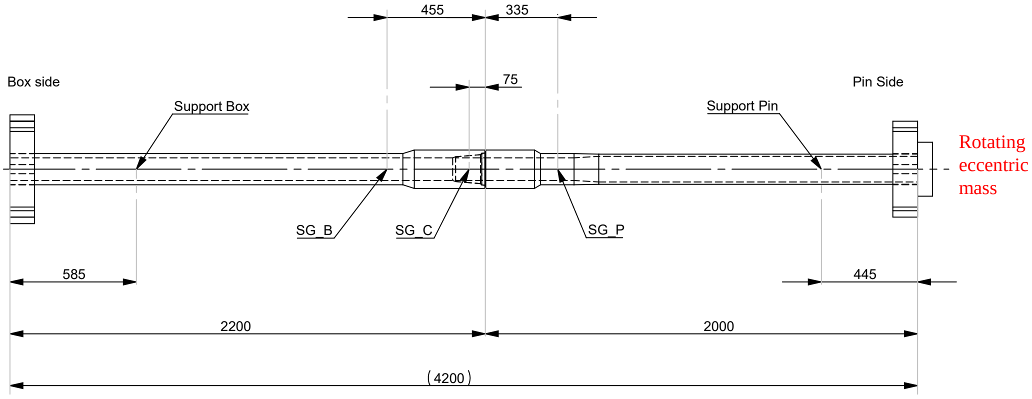

(c) Wired connection with 5×0.374″ pipe body - S135

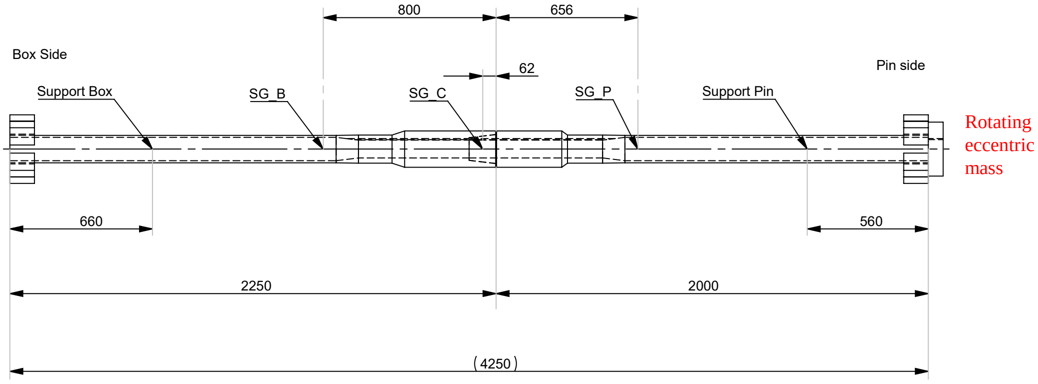

Figure 7. (**a**) Connection with 5-1/2×0.415″ pipe body—Regular upset, (**b**) Connection with 5-1/2×0.415″—Longer upset, (**c**) Wired Connection with 5×0.374″ pipe body.

(a) Connection with 6-5/8×0.750″ pipe body, UD165

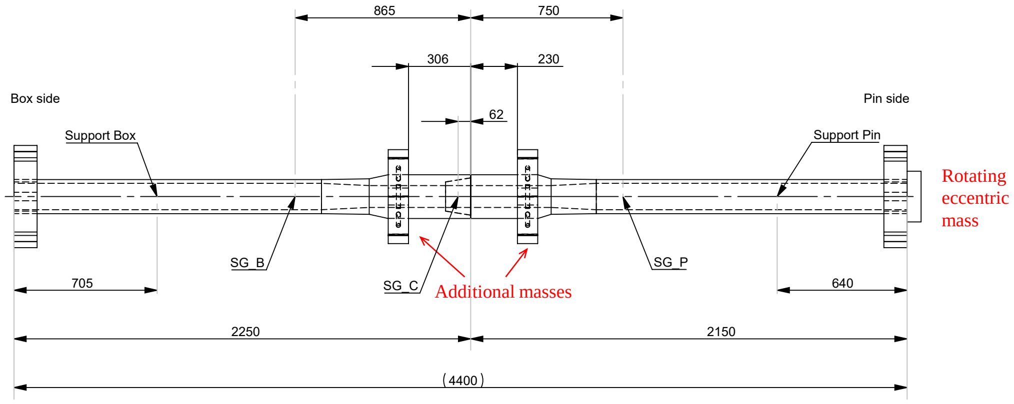

(b) Connection with 6-5/8×0.750″ pipe body, Z140

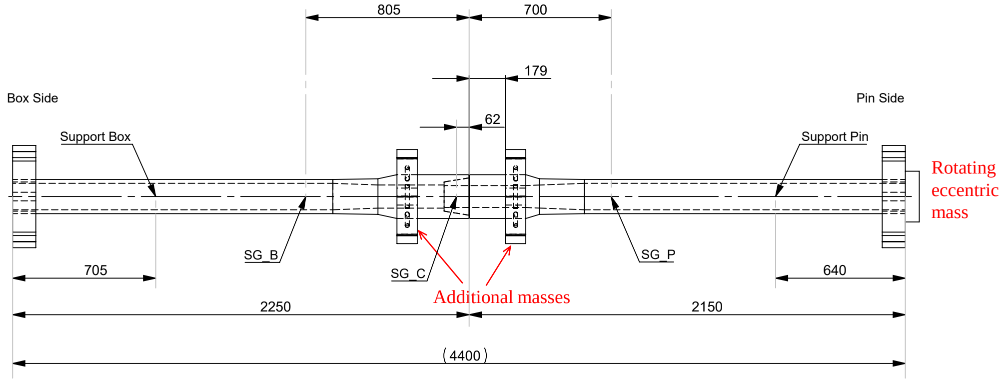

(c) Pipe Specimen 6-5/8×0.750″, UD165/Z140

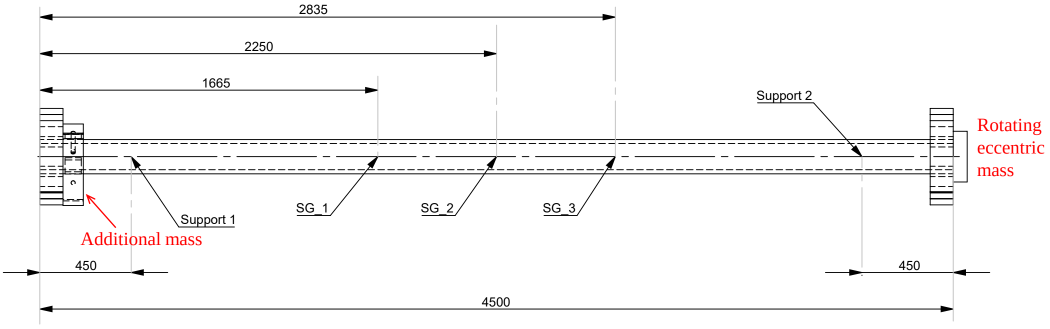

Figure 8. (**a**) Connection with 6-5/8×0.750″ pipe body, UD165, (**b**) Connection with 6-5/8×0.750″ pipe body, Z140, (**c**) Pipe specimen 6-5/8″ Z140 and UD165 and application of additional masses to both the connection and the pipe specimens for lowering the first natural frequency.

(a) Connection with 5-1/2×0.415″ pipe body - AISI 4130 - Regular upset (b) Connection with 5-1/2×0.415″ pipe body - AISI 4130 - Longer upset

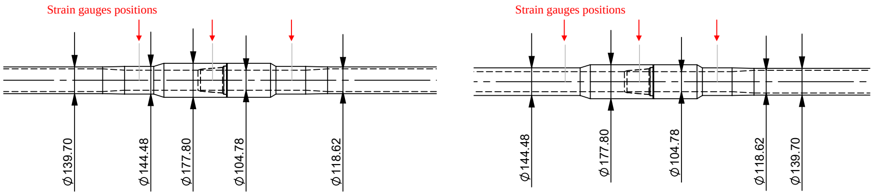

(c) Wired connection with 5×0.374″ pipe body- S135 (d) Connection with 6-5/8×0.750″ pipe body UD165 (Z140)

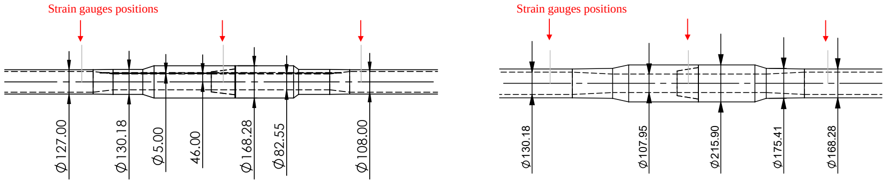

Figure 9. External and internal diameters of: (**a**) Connection with 5-1/2×0.415″ pipe body—Regular upset, (**b**) Connection with 5-1/2×0.415″—Longer upset, (**c**) Wired Connection with 5×0.374″ and (**d**) Connection with 6-5/8×0.750″ pipe body.

3. Results

The fatigue crack initiation regions are listed in Table 1 for each type of connection. The Connection specimens with 5-1/2×0.415″ pipe body and the Connection with 6-5/8×0.750″ pipe body, failed at the FET of the pin side, whereas the failure of the Wired Connection samples was located at the pipe body. The fatigue test results of each specimen are also reported in Table 1 in terms of the stress amplitude and the number of cycles to failure. As mentioned before, the strain gauges were placed on the upset zone for the Connection with 5-1/2×0.415″ pipe body while at the pipe body for all the other geometries. The imposed amplitude stress in correspondence with the pipe body of the specimens was $\sigma_{a,ref} = 270$ MPa. In order to keep the same stress amplitude at the pipe body, the target stress to be imposed at the upset region was rescaled by means of the beam theory combined with the modal distribution of the bending moment. The numerical values of the stress amplitude presented in Table 1 are referred to the imposed alternating stress at the pipe body, about the connection samples with 6-5/8×0.750″ pipe body, and to the stress at the upset region regarding the Connection with 5-1/2×0.415″ pipe body. On the other hand, the values of the stress amplitude of the Wired Connection samples, reported in Table 1, substantially differ from the nominal $\sigma_{a,ref} = 270$ MPa because the measured values of the internal diameters obtained at the end of the tests were different from the nominal ones and, in addition to this, the locations of the fatigue cracks were not exactly in correspondence of the strain gauges positions. The bending moment at the initiation positions was lower than that at the strain gauges, so the material was expected to be not perfectly uniform; otherwise, the failure would have been obtained near the upset region where the load is higher. According to this, the bending moment acting on the section corresponding to the failure was obtained from that at the strain gauge location, and a rescale factor was calculated from the modal FE distribution of the bending moment. The fatigue strength data of the tested samples of all the geometries involved in this research, and that of the previous tests presented in ref. [43] (for comparison), are reported in Figure 10. In addition to the S-N data, fractographic images about the initiations and subsequent propagations of the cracks are shown in Figure 11 for all the drill pipe connection types involved in this research.

An FE model was implemented to investigate the effect of the through hole on the structural strength of the Wired Connection, and the results are presented in Figure 12. As shown in this figure, a Global FE model was initially solved after applying a bending moment corresponding to one of the fatigue tests, while a fixed support was applied on the other side. A Submodel of the transaction region between the pipe body and the upset was then implemented, as shown in Figure 12b. Both the Global model and the Submodel exploited one plane of symmetry. The loading displacements then applied to the Submodel were obtained at the interface surfaces by interpolating the Global model. Both the Global and the Submodel maps of the axial stress, Figure 12a,b, show that the maximum is located far from the hole zone. The distribution of the axial stress obtained from the Submodel was extracted along a path on the hole's internal surface, and it is shown in Figure 12c where it is evident the absence of a high gradient stress concentration. The FE analysis presented in Figure 12 clearly shows that the presence of the hole was, therefore, not detrimental to the fatigue strength of the Wired Connection samples. In Figure 10, which compares all the results with previous tests, it is shown that the samples belonging to the Wired Connection type and those of the Connection with 6-5/8×0.750″ pipe body (both Z140 and UD165), together with the samples referred to the previous tests of ref. [43], follow a common trend of fatigue failure. On the other hand, the samples of the connection type with 5-1/2×0.415″ pipe body showed a noticeably higher fatigue strength than the common trend of the other specimens. Moreover, the samples belonging to the category Pipe specimens 6-5/8×0.750″ failed at a number of cycles higher than that of the samples of the connection with the same size pipe body. This is coherent with the fact that the connection specimens experienced failures at the threaded zone, which is indeed the weakest link of the entire specimen structure. An additional detrimental effect on the fatigue strength of the former samples, discussed by Santus et al. in ref. [43], was provided by the corrosion, whereas it apparently less influenced the fatigue strength of the present Pipe specimens 6-5/8×0.750″. It is important to highlight that the values of the imposed stress amplitude on the Connection with 5-1/2×0.415″ pipe body reported in Table 1 are referred to the upset region, whereas those reported in Figure 10 are referred to the pipe body. The rescale factor between these two values was obtained by considering the modal distribution of the bending moment and the different sections of the two zones.

Table 1. Fatigue strength amplitude and number of cycles to failure for each sample of the four specimens types.

Specimen Type	Specimen ID	Imposed Stress Amplitude σ_a (MPa)	Number of Cycles to Failure, N_f	Location of Crack Initiation Point
Connection with 5-1/2″ pipe body	RU W0581-1	187.3	279.7×10^3	FET of the Pin side
	RU W0581-2	191.5	291.0×10^3	
	LU W0579-1	194.6	247.3×10^3	
	LU W0582-1	187.1	310.0×10^3	
Wired Connection with 5″ pipe body	A51136	202.2	135.9×10^3	Pipe body
	A51155	201.9	218.7×10^3	
	A51168	194.9	214.7×10^3	
	A51167	244.6	439.0×10^3	
	A51140	242.8	272.5×10^3	
	A51119	191.7	220.9×10^3	
Connection with 6-5/8″ pipe body	Z140-14012	270	47.9×10^3	FET of the Pin side
	Z140-14030	270	116.3×10^3	
	Z140-14041	270	99.2×10^3	
	Z140-14076	270	116.9×10^3	
	Z140-14099	270	110.5×10^3	
	Z140-14110	270	116.5×10^3	
	UD165-9250	270	922.0×10^3	
	UD165-49267	270	107.5×10^3	
	UD165-49218	270	109.5×10^3	
	UD165-49221	270	136.7×10^3	
	UD165-9257	270	96.7×10^3	
Pipe specimens 6-5/8″	UD165-49267	270	256.5×10^3	Pipe body
	Z140-14076	270	238.5×10^3	

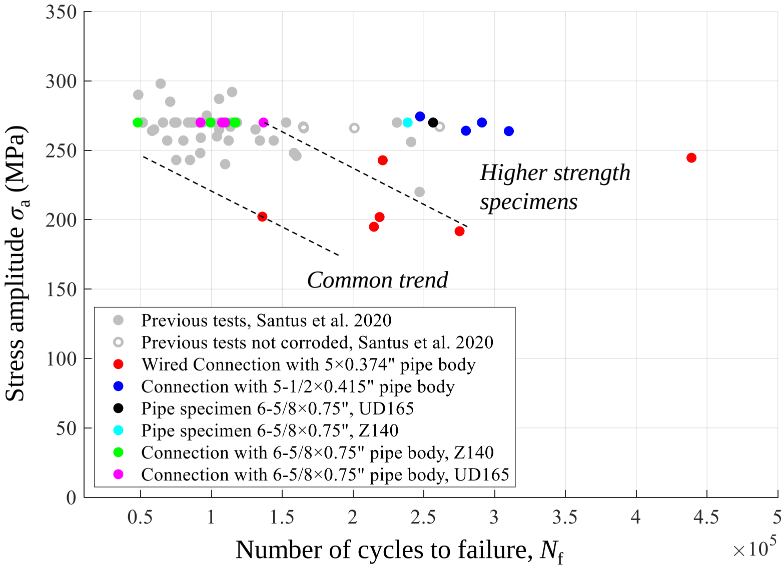

Figure 10. Fatigue strength data of all the presented and tested samples compared with the data obtained during a previous testing campaign [43].

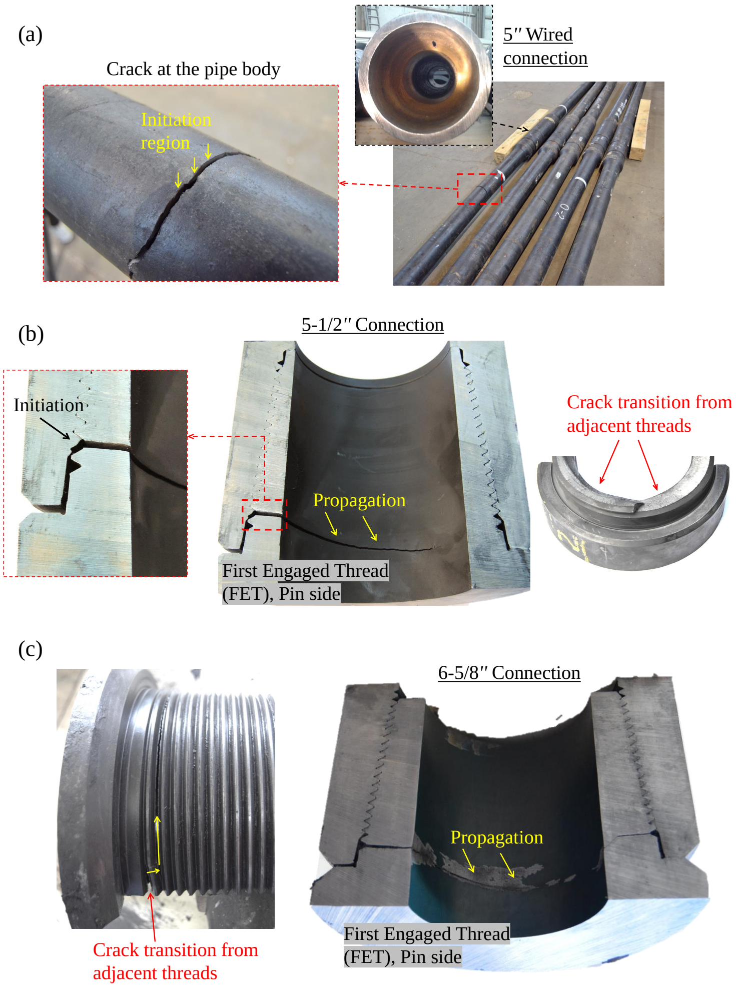

Figure 11. Fractographic images of (**a**) crack initiation at the pipe body of the Wired Connection with 5×0.374″ pipe body, (**b**) crack initiation and propagation at the FET (pin side) of the Connection with 5-1/2×0.415″ pipe body and (**c**) crack initiation and propagation at the FET (pin side) of the Connection with 6-5/8×0.750″ pipe body.

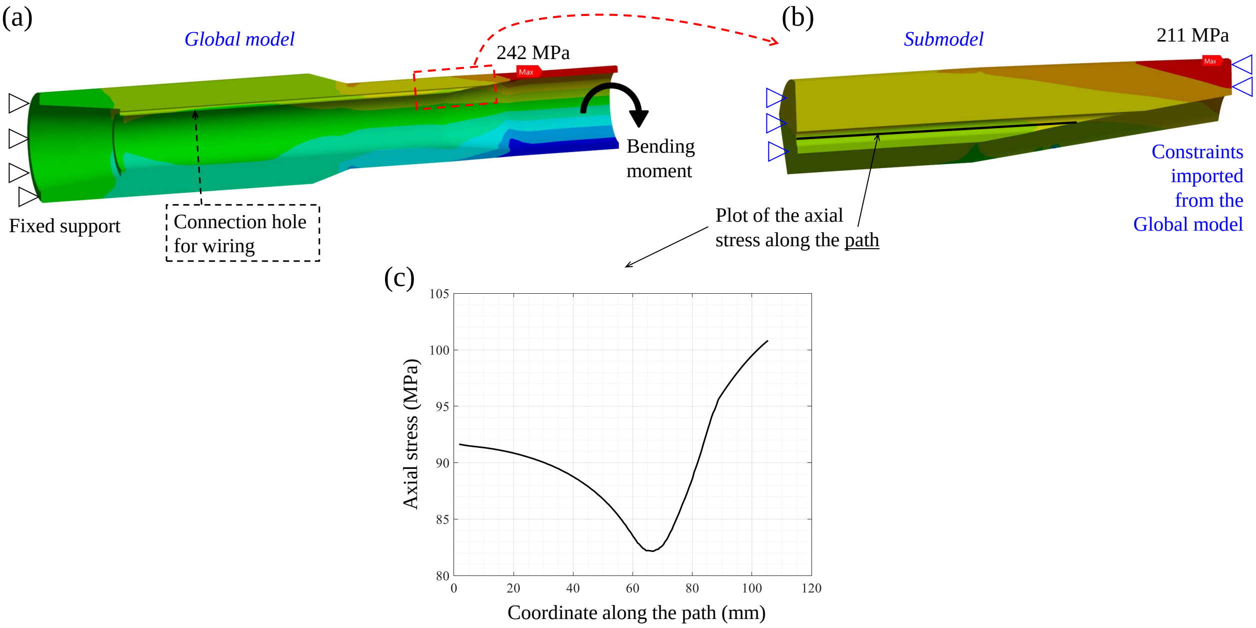

Figure 12. (**a**) FE map of the axial stress of the Global model, (**b**) map of the axial stress of the Submodel, and (**c**) plot of the axial stress along the path realized through the hole.

4. Discussion

The comparison of different connections and sizes put in evidence how the ratio between the section modulus of bending (namely $\pi(D_{\mathrm{ext}}^4 - D_{\mathrm{int}}^4)/32D_{\mathrm{ext}}$), between connection, upset region, and pipe body, has a significant role in driving the position of fatigue crack initiation. It is worth noting that the modulus of bending depends on the cubic power of the external diameter, and also the internal one has a significant role. This justifies the employment of accurate instruments to obtain the true dimensions of the internal and external diameters. The fatigue crack is more prone to initiate at the connection, in particular at the FET of the pin, whenever the bending modulus at the connection is just slightly larger than that of the pipe body, and then the stress concentration at the thread root can be critical. On the contrary, the Wired Connection, which features a larger bending modulus, resulted in a safer condition than the pipe body, even with a passing-through hole, as evident in the present fatigue campaign. The trends of the bending moment, corresponding to the imposed amplitude stresses during the tests, for all kinds of the geometries investigated, are reported in Figures 13 and 14, along with the corresponding nominal bending stress amplitude at the various zones of the drill pipe, calculated with the beam theory. Points A, B and C are generally referred to the pipe body, the upset region and the connection region, respectively, while points A′ and B′ are the symmetric of A and B. In the Connection with 5-1/2×0.415″ pipe body—Longer upset, point A is referred to the upset region, point B to the connection region and point C to the pipe body, while A′ is the symmetric of A. It can be noticed that the Wired Connection drill pipes experience the highest value of the ratio between the maximum bending stress amplitude at the pipe body and the maximum nominal bending stress amplitude at the connection. This ratio is higher than three, mainly due to the much larger outer diameter at the connection. In ref. [55], the stress concentration factor for connection geometries, similar to the wired tool joint samples of this study, was calculated through a 3D FE model. The obtained values of the stress concentration factor fell into the range between two and three, so this can justify the failure at the pipe body instead of at the connection. The corrosion state of the pipe can play a significant role in steering the crack initiation. The Connection with 5-1/2×0.415″ pipe body tested in the present fatigue campaign reported the fatigue initiation at the connection (pin FET). However, a similar connection was previously tested on connection specimens with corroded pipe bodies, and results are reported for a comparison in Figure 10, as previously discussed.

The failures of these former tests were observed at the pipe bodies since the connection surfaces were properly coated and then not affected by corrosion. On the contrary, the latter specimens reported an appreciably higher strength and failure at the connection instead of the pipe body. A longer upset was also tested, for comparison with respect to the standard geometry, in which the upset has a regular (short) length. An evident result was that the failure remained at the connection pin FET and approximately at the same fatigue life. Therefore, the main conclusion that can be formulated is that the longer upset manufacturing did not produce any detrimental effect on the material and its fatigue strength of the connection. Large-size specimens were also tested (6-5/8×0.750″). Among the specimens of this size category, two grades were investigated, namely 140 ksi and 165 ksi, which define the (minimum) yield strength. Despite this appreciable grade difference, the fatigue strengths that resulted were quite similar. This evidence can be explained by considering that after a certain (static) strength, the fatigue of the steel does not keep increasing linearly with the yield stress or the ultimate tensile strength.

(a) Connection with 5-1/2×0.415″ pipe body - AISI 4130 - Regular upset

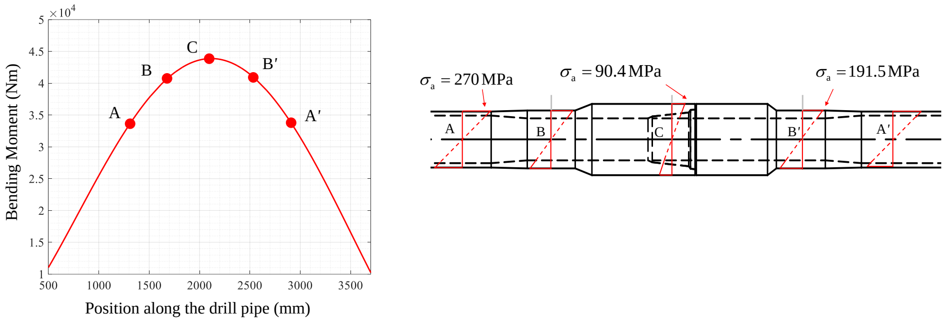

(b) Connection with 5-1/2×0.415″ pipe body - AISI 4130 - Longer upset

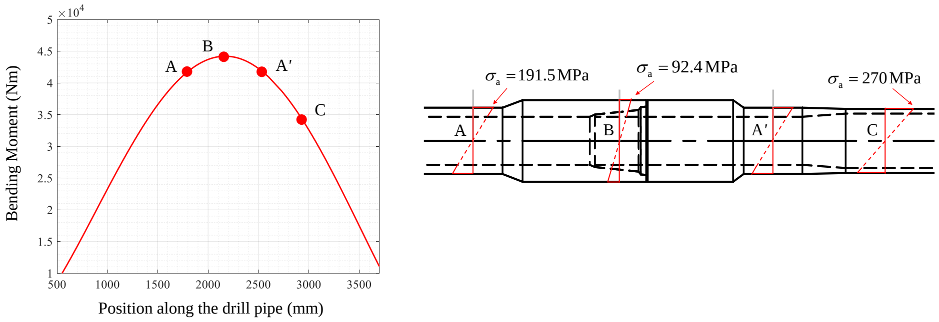

(c) Connection with 6-5/8×0.750″ pipe body, UD165

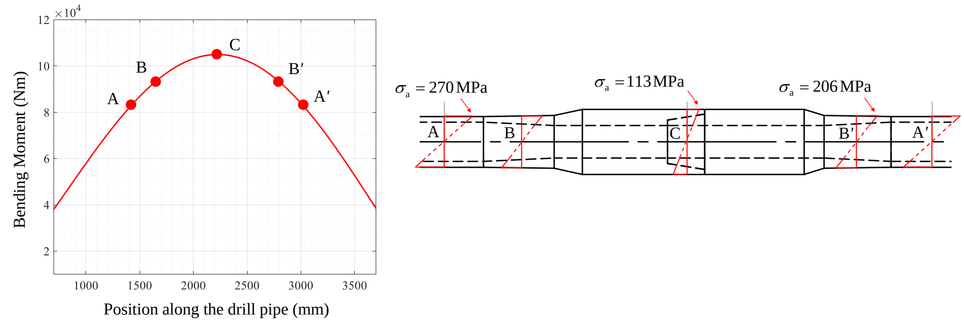

Figure 13. Bending moment with corresponding beam theory maximum nominal amplitude bending stress of: (**a**) Connection with 5-1/2×0.415″ pipe body—Regular upset, (**b**) Connection with 5-1/2×0.415″ pipe body—Longer upset and (**c**) Connection with 6-5/8×0.750″ pipe body, UD165.

(a) Connection with 6-5/8×0.750″ pipe body, Z140

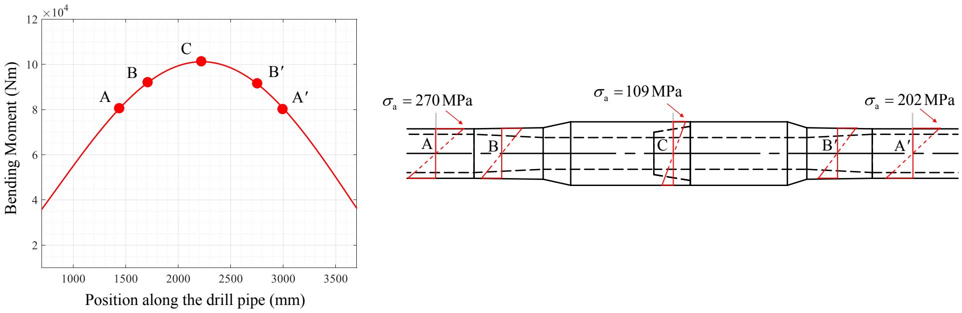

(b) Wired Connection with 5×0.374″ pipe body - S135

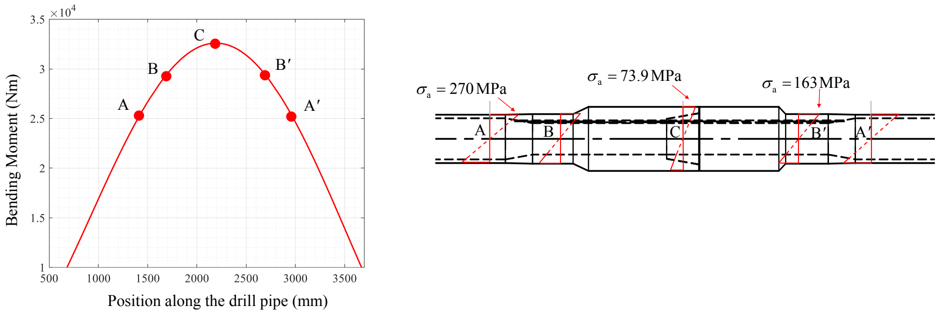

(c) Wired Connection with 5×0.374″ pipe body - S135 – True dimensions

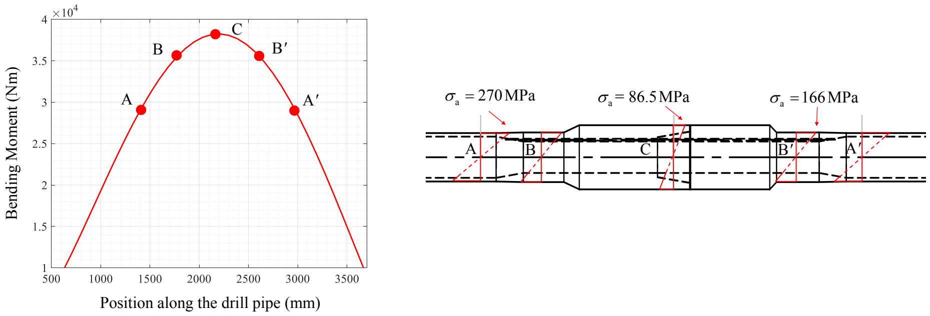

Figure 14. Bending moment with corresponding beam theory maximum nominal amplitude bending stress of: (**a**) Connection with 6-5/8×0.750″ pipe body, Z140, (**b**) Wired Connection with 5×0.374″ pipe body and (**c**) Wired Connection with 5×0.374″ pipe body—True dimensions.

5. Conclusions

In the present paper, a resonant test bench is presented along with four series of tests with different connection geometries and sizes. This test rig is based on the principle of resonance, which is quite efficient in enhancing the working test frequency and avoiding a heavy structure to produce a static load with a closed path. Several aspects of the testing procedure are presented in detail in the first part of the paper. Accurate testing requires a calibration of the strain gauges, and this can be performed statically with a dedicated procedure and an actuator with a calibrated load cell. However, attention must be paid to the actual diameters of the sections to which the strain gauges are attached. The external diameter can be easily measured with a common caliper, while a remotely adjustable comparator was devised and produced for the internal diameter measurement. After using this tool, the actual bending modulus can be accurately evaluated at the calibration stage. A specific control system was also designed and implemented by creating and interfacing different electronic devices, and then to have a closed-loop control on either the stress amplitude (at the strain gauge positions) or the laser vibration amplitude. The control in terms of the stress amplitude was obviously preferential after the accurate calibration previously mentioned. However, the control on the displacement amplitude, which was measured by contactless laser sensors, was assumed whenever the strain gauge experienced damage, which can be attributed to the fatigue itself of the strain gauge grid, being the strain amplitude quite large during these tests. The fatigue results highlighted that three out of four connection drill pipes failed at the FET of the threaded zone, whereas just one failed at the pipe body. This comparison highlighted the great role of the section modulus of bending in driving the fatigue failure; in fact, for the wired connection samples, which presented a massive section at the connection zone, the failure was located at the pipe body. A more comprehensive study of the connection zone could be performed, in future work, by means of FE analyses and eventually involving the modeling of the cyclic plastic behavior of the steel, in particular at the thread root of the FET. After a material calibration, for example, by following the procedure proposed in ref. [56] to find the Chaboche kinematic hardening rule constants, the possible thread root relaxation can be modeled, and investigated in terms of the applied Make-Up torque preload, to obtain a more direct comparison between the loading condition at the pin FET and the pipe body.

Author Contributions: Conceptualization, C.S., L.R. and A.B.; methodology, C.S., L.R. and A.B.; software, A.B.; validation, C.S., L.R. and T.I.; formal analysis, C.S. and L.R.; investigation, C.S., L.R. and A.B.; resources, C.S., L.R., A.B. and T.I.; data curation, C.S., L.R. and A.B.; writing—original draft preparation, C.S., L.R. and T.I.; writing—review and editing, C.S., L.R. and T.I.; visualization, C.S. and L.R.; supervision, T.I.; project administration, C.S., L.R. and T.I.; funding acquisition, T.I. All authors have read and agreed to the published version of the manuscript.

Funding: This research received no external funding.

Data Availability Statement: Data are contained within the article.

Conflicts of Interest: The authors declare no conflict of interest.

Abbreviations

The following abbreviations are used in this manuscript:

API	American Petroleum Institute
FE	Finite Element
FET	First engaged thread
LET	Last engaged thread
PI	Proportional Integrative
PWM	Pulse-width modulation
RU	Regular Upset
LU	Longer Upset
SG_B	Strain gauge at the box
SG_C	Strain gauge at the connection
SG_P	Strain gauge at the pin

References

1. API Specification. *Specification for Rotary Drill Stem Elements*; American Petroleum Institute: Washington, DC, USA, 2006.
2. Inoue, T.; Wada, K.; Miyazaki, E.; Miyazaki, T. Scientific Drilling Program of Drilling Vessel Chikyu and Drilling Data Acquisition for Future Technical Development. In Proceedings of the Volume 5: Ocean Space Utilization Ocean Renewable Energy, ASMEDC, Rotterdam, The Netherlands, 19–24 June 2011. [CrossRef]
3. Inoue, T.; Kyo, M.; Sakura, K. Fatigue Strength Evaluation of Drill Pipe for Challenging Deep Drilling Project—Japan Trench Fast Drilling (JFAST). In Proceedings of the International Ocean and Polar Engineering Conference, Anchorage, Alaska, 30 June–5 July 2013; ISOPE-I-13-224.
4. Zamani, S.M.; Hassanzadeh-Tabrizi, S.A.; Sharifi, H. Failure analysis of drill pipe: A review. *Eng. Fail. Anal.* **2016**, *59*, 605–623. [CrossRef]
5. Rahman, M. Stress concentration incorporated fatigue analysis of die-marked drill pipes. *Int. J. Fatigue* **1999**, *21*, 799–811. [CrossRef]
6. Rahman, M.K.; Hossain, M.M.; Rahman, S.S. Survival assessment of die-marked drill pipes:. *Eng. Fail. Anal.* **1999**, *6*, 277–299. [CrossRef]
7. Zhu, H.; Lin, Y.; Zeng, D.; Zhou, Y.; Xie, J. Simulation analysis of flow field and shear stress distribution in internal upset transition zone of drill pipe. *Eng. Fail. Anal.* **2012**, *21*, 67–77. [CrossRef]

8. Liu, Y.; Li, F.; Xu, X.; Yang, B.; Lu, C. Simulation Technology in Failure Analysis of Drill Pipe. *Procedia Eng.* **2011**, *12*, 236–241. [CrossRef]
9. Lin, Y.; Qi, X.; Zhu, D.; Zeng, D.; Zhu, H.; Deng, K.; Shi, T. Failure analysis and appropriate design of drill pipe upset transition area. *Eng. Fail. Anal.* **2013**, *31*, 255–267. [CrossRef]
10. Lu, S.; Feng, Y.; Luo, F.; Qin, C.; Wang, X. Failure analysis of IEU drill pipe wash out. *Int. J. Fatigue* **2005**, *27*, 1360–1365. [CrossRef]
11. Luo, S.; Wu, S. Effect of stress distribution on the tool joint failure of internal and external upset drill pipes. *Mater. Des.* **2013**, *52*, 308–314. [CrossRef]
12. Lubinski, A. Maximum Permissible Dog-Legs in Rotary Boreholes. *J. Pet. Technol.* **1961**, *13*, 175–194. [CrossRef]
13. MacDonald, K.A. Failure analysis of drillstring and bottom hole assembly components. *Eng. Fail. Anal.* **1994**, *1*, 91–117. [CrossRef]
14. Tafreshi, A.; Dover, W. Stress analysis of drillstring threaded connections using the finite element method. *Int. J. Fatigue* **1993**, *15*, 429–438. [CrossRef]
15. Macdonald, K.A. The effectiveness of stress relief features in austenitic drillcollar connections. *Eng. Fail. Anal.* **1996**, *3*, 267–279. [CrossRef]
16. Macdonald, K.A.; Deans, W.F. Stress analysis of drillstring threaded connections using the finite element method. *Eng. Fail. Anal.* **1995**, *2*, 1–30. [CrossRef]
17. Vaisberg, O.; Vincké, O.; Perrin, G.; Sarda, J.P.; Fay, J.B. Fatigue of Drillstring: State of the Art. *Oil Gas Sci.-Technol.-Rev. Inst. Fr. Pet.* **2002**, *57*, 7–37. [CrossRef]
18. Macdonald, K.A.; Bjune, J.V. Failure analysis of drillstrings. *Eng. Fail. Anal.* **2007**, *14*, 1641–1666. [CrossRef]
19. Albdiry, M.T.; Almensory, M.F. Failure analysis of drillstring in petroleum industry: A review. *Eng. Fail. Anal.* **2016**, *65*, 74–85. [CrossRef]
20. Ferjani, M.; Averbuch, D.; Constantinescu, A. A computational approach for the fatigue design of threaded connections. *Int. J. Fatigue* **2011**, *33*, 610–623. [CrossRef]
21. Zarka, J. *A New Approach in Inelastic Analysis of Structures*; Laboratoire de Mecanique des Solides: Palaiseau, France, 1990.
22. Lin, T.; Zhang, Q.; Lian, Z.; Liu, Y.; Zhang, Y.; Chen, Y. Multi-axial fatigue life prediction of drill collar thread in gas drilling. *Eng. Fail. Anal.* **2016**, *59*, 151–160. [CrossRef]
23. Santus, C.; Bertini, L.; Burchianti, A.; Inoue, T.; Sakurai, N. Fatigue resonant tests on drill collar rotary shouldered connections and critical thread root identification. *Eng. Fail. Anal.* **2018**, *89*, 138–149. [CrossRef]
24. Wittenberghe, J.V.; Baets, P.D.; Waele, W.D.; Galle, T.; Bui, T.T.; Roeck, G.D. Design characteristics that improve the fatigue life of threaded pipe connections. *Int. J. Sustain. Constr. Des.* **2011**, *2*, 334–341. [CrossRef]
25. Liu, H.; He, Y.; Wan, J.; Chen, L.; Yi, X.; Hou, S.; Wang, Y.; He, D.; Li, G. New design method of unequal taper thread (UTT) pairs and its application in API NC38 thread improvement. *Petroleum* **2023**, *in press*. [CrossRef]
26. Korin, I.; Ipiña, J.P. Controlled residual stresses introduction to improve fatigue resistance of rotary shouldered connections used in oil drilling industry. *Int. J. Press. Vessel. Pip.* **2010**, *87*, 696–703. [CrossRef]
27. Moradi, S.; Ranjbar, K. Experimental and computational failure analysis of drillstrings. *Eng. Fail. Anal.* **2009**, *16*, 923–933. [CrossRef]
28. Inoue, T.; Ozaki, M.; Miyazaki, T.; Nishigaki, M.; Setta, K. Fatigue strength evaluationof drill pipe constantly bent in strong current. In Proceedings of the 8th 2008 ISOPE Pacific/Asia Offshore Mechanics Symposium, Bangkok, Thailand, 10–14 November 2008.
29. Inoue, T.; Kyo, M.; Sakura, K.; Fukui, T. Fatigue Strength Investigation of Drill Pipe for Challenging Scientific Deep Drilling and Utilization of Drilling Data to Estimate Cumulative Fatigue. In Proceedings of the Offshore Technology Conference, Houston, TX, USA, 5–8 May 2014. [CrossRef]
30. Baryshnikov, A.; Calderoni, A.; Ligrone, A.; Ferrara, P. A New Approach to the Analysis of Drillstring Fatigue Behavior. *SPE Drill. Complet.* **1997**, *12*, 77–84. [CrossRef]
31. Hakimi, H.; Moradi, S. Drillstring vibration analysis using differential quadrature method. *J. Pet. Sci. Eng.* **2010**, *70*, 235–242. [CrossRef]
32. Besselink, B.; van de Wouw, N.; Nijmeijer, H. A Semi-Analytical Study of Stick-Slip Oscillations in Drilling Systems. *J. Comput. Nonlinear Dyn.* **2010**, *6*, 021006 . [CrossRef]
33. Kessai, I.; Benammar, S.; Doghmane, M.Z.; Tee, K.F. Drill Bit Deformations in Rotary Drilling Systems under Large-Amplitude Stick-Slip Vibrations. *Appl. Sci.* **2020**, *10*, 6523. [CrossRef]
34. Wada, R.; Kaneko, T.; Ozaki, M.; Inoue, T.; Senga, H. Longitudinal natural vibration of ultra-long drill string during offshore drilling. *Ocean. Eng.* **2018**, *156*, 1–13. [CrossRef]
35. Kulke, V.; Thunich, P.; Schiefer, F.; Ostermeyer, G.P. A Method for the Design and Optimization of Nonlinear Tuned Damping Concepts to Mitigate Self-Excited Drill String Vibrations Using Multiple Scales Lindstedt-Poincaré. *Appl. Sci.* **2021**, *11*, 1559. [CrossRef]
36. Riane, R.; Doghmane, M.Z.; Kidouche, M.; Tee, K.F.; Djezzar, S. Stick-Slip Vibration Suppression in Drill String Using Observer-Based LQG Controller. *Sensors* **2022**, *22*, 5979. [CrossRef]
37. Teodoriu, C. Oil Country Tubular Goods Fatigue Testing: Do We Test Them Enough? In Proceedings of the Volume 4: Materials Technology. American Society of Mechanical Engineers, Trondheim, Norway, 25–30 June 2017. [CrossRef]

38. Miscow, G. Techniques to characterize fatigue behaviour of full size drill pipes and small scale samples. *Int. J. Fatigue* **2004**, *26*, 575–584. [CrossRef]
39. Bertini, L.; Beghini, M.; Santus, C.; Baryshnikov, A. Resonant test rigs for fatigue full scale testing of oil drill string connections. *Int. J. Fatigue* **2008**, *30*, 978–988. [CrossRef]
40. Haagensen, P.J.; Grøttum, T.I. Fatigue Assessment of Drill Pipes. In Proceedings of the Volume 4: Materials Technology. American Society of Mechanical Engineers, Trondheim, Norway, 25–30 June 2017. [CrossRef]
41. Oku, Y.; Sugino, M.; Ando, Y.; Makino, T.; Komoda, R.; Takazaki, D.; Kubota, M. Fretting fatigue on thread root of premium threaded connections. *Tribol. Int.* **2017**, *108*, 111–120. [CrossRef]
42. Wittenberghe, J.V.; Baets, P.D.; Waele, W.D.; Ost, W.; Verstraete, M.; Hertelé, S. Resonant Bending Fatigue Test Setup for Pipes With Optical Displacement Measuring System. *J. Offshore Mech. Arct. Eng.* **2012**, *134*. [CrossRef]
43. Santus, C.; Burchianti, A.; Inoue, T.; Ishiguro, H. Fatigue resonant tests on S140 and S150 grade corroded drill pipe connections and pipe bodies. *Int. J. Press. Vessel. Pip.* **2020**, *184*, 104107. [CrossRef]
44. Schneider, S.; Herrmann, R.; Marx, S. Development of a resonant fatigue testing facility for large-scale beams in bending. *Int. J. Fatigue* **2018**, *113*, 171–183. [CrossRef]
45. Chuan, W.; Zhu, H.; Wang, D. Test System and Model for Fatigue Performance Evaluation of Marine Riser. *J. Appl. Sci.* **2013**, *13*, 854–861. [CrossRef]
46. Xiaoming, F.; Zhichao, Y.; Liquan, W.; Yuxuan, H. Experiment and Finite Analysis on Resonant Bending Fatigue of Marine Risers. *Open Mech. Eng. J.* **2015**, *9*, 205–212. [CrossRef]
47. Snowberg, D.; Dana, S.; Hughes, S.; Berling, P. *Implementation of a Biaxial Resonant Fatigue Test Method on a Large Wind Turbine Blade*; Technical Report; National Renewable Energy Lab. (NREL): Golden, CO, USA, 2014. [CrossRef]
48. Melcher, D.; Bätge, M.; Neßlinger, S. A novel rotor blade fatigue test setup with elliptical biaxial resonant excitation. *Wind. Energy Sci.* **2020**, *5*, 675–684. [CrossRef]
49. Yun, G.J.; Abdullah, A.B.M.; Binienda, W. Development of a Closed-Loop High-Cycle Resonant Fatigue Testing System. *Exp. Mech.* **2011**, *52*, 275–288. [CrossRef]
50. Feng, M.; Li, M. Development of a Computerized Electrodynamic Resonant Fatigue Test Machine and Its Applications to Automotive Components; SAE Technical Paper Series; SAE International: Warrendale, PA, USA, 2003. [CrossRef]
51. Huertas, J.I.; Navarrete, N.; Giraldo, M.; Uribe, J.D.; Gasca, J.J. Resonant fatigue test bench for shaft testing. *Fatigue Fract. Eng. Mater. Struct.* **2016**, *40*, 364–374. [CrossRef]
52. Thomas, C.; Sainz-Aja, J.; Setien, J.; Cimentada, A.; Polanco, J.A. Resonance fatigue testing on high-strength self-compacting concrete. *J. Build. Eng.* **2021**, *35*, 102057. [CrossRef]
53. Okeke, C.P.; Thite, A.N.; Durodola, J.F.; Greenrod, M.T. A novel test rig for measuring bending fatigue using resonant behaviour. *Procedia Struct. Integr.* **2018**, *13*, 1470–1475. [CrossRef]
54. Mitu, A.M.; Sireteanu, T.; Pop, N.; Chis, L.C.; Maxim, V.M.; Apsan, M.R. Numerical and Experimental Study of the Fatigue Behavior for a Medical Rehabilitation Exoskeleton Device Using the Resonance Method. *Materials* **2023**, *16*, 1316. [CrossRef]
55. Shahani, A.R.; Sharifi, S.M.H. Contact stress analysis and calculation of stress concentration factors at the tool joint of a drill pipe. *Mater. Des.* **2009**, *30*, 3615–3621. [CrossRef]
56. Santus, C.; Grossi, T.; Romanelli, L.; Pedranz, M.; Benedetti, M. A computationally fast and accurate procedure for the identification of the Chaboche isotropic-kinematic hardening model parameters based on strain-controlled cycles and asymptotic ratcheting rate. *Int. J. Plast.* **2023**, *160*, 103503. [CrossRef]